Available online at https://link.springer.com/journal/42241
http://www.jhydrodynamics.com
Journal of Hydrodynamics, 2026
https://doi.org/10.1007/s42241-026-0077-y

LES investigation of wall fluctuating pressure over a prolate spheroid with tripping at angles of attack

Lei-xuan Liu[1], Lu-chun Yang[2], Wei-wen Zhao[1], De-cheng Wan[1*]

1. *Computational Marine Hydrodynamics Lab (CMHL), School of Ocean and Civil Engineering, Shanghai Jiao Tong University, Shanghai 200240, China*
2. *Wuhan Second Ship Design and Research Institute, Wuhan 430064, China*

(Received June 4, 2026, Revised July 9, 2026, Accepted July 9, 2026, Published online October 14, 2026)
©China Ship Scientific Research Center 2026

Abstract: As a typical non-streamlined bluff body, a prolate spheroid has wall fluctuating pressure changes that are very important for structural fatigue damage, flow-induced vibration, and noise control. It is widely used in aerospace and ocean engineering. This paper studies a prolate spheroid with an aspect ratio of 6:1. It uses numerical simulation to find how the wall fluctuating pressure changes under high Reynolds number flow. A physical trip wire is used to make sure the flow becomes turbulent. Large eddy simulation (LES) is used to capture turbulent structures and wall fluctuating pressure signals. The Reynolds number is 4.2×10^6, with angles of attacks (AOAs, i.e. α) of the prolate spheroid covering the range from $0°$ to $20°$. The spatial distribution, time evolution, and development trend of wall fluctuating pressure are studied under different AOAs.

Key words: Turbulent boundary layer, wall fluctuating pressure, physical tripwire, angle of attack (AOA)

0. Introduction

Accurate prediction of the maneuverability and hydrodynamic characteristics of submarines and underwater vehicles depends largely on an in-depth understanding of the flow field around the main body[1]. The geometric shape of the 6:1 prolate spheroid is highly consistent with the main contour of the real underwater vehicle, so it has become a classical reference model for studying the flow around such axisymmetric bodies[2-3]. When the model is in an inclined state, the flow field around it will show strong nonlinear physical phenomena, including three-dimensional boundary layer transition, cross-flow separation, and the generation and evolution of multi-scale vortices. These processes directly determine the wall pressure distribution and the overall hydrodynamic load of the model[4]. In addition, the secondary flow induced by streamline curvature and circumferential asymmetric wall pressure gradient will significantly change the transition path and separation characteristics of the boundary layer[5]. This phenomenon leads to the complex evolution of wall pressure in time and space. The amplitude, spatial distribution, and spectral characteristics of the wall pressure fluctuation are the core input parameters for analyzing structural vibration and predicting flow-induced noise, which is a common fundamental issue across multiple hydrodynamic engineering fields[6]. Therefore, in-depth research in this field has important engineering and academic value for the acoustic stealth design and maneuverability optimization of underwater vehicles[7].

Over the past few decades, scholars have systematically investigated the flow around inclined 6:1 prolate spheroids. Figure 1 shows the geometry of the 6:1 prolate spheroid model. In experimental studies, Chesnakas and Simpson[2] detailed the three-dimensional separation region at $10°$ and $30°$ inclinations, clarifying the initiation of cross-flow separation and the evolution of main vortex pairs. Fu et al.[8] utilized flow visualization to demonstrate that increased inclination triggers earlier separation, with counter-rotating streamwise vortices governing wake development. Meier and Kreplin[9] identified distinct windward transition mechanisms, while Wetzel[10] observed separation hysteresis during unsteady maneuvers, highlighting the need for highly accurate unsteady flow simulations. In numerical research,

Project supported by the National Natural Science Foundation of China (Grant No. 52131102).
Biography: Lei-xuan Liu (2001-), Male, Master,
E-mail: 3308132783@qq.com
Corresponding author: De-cheng Wan,
E-mail: dcwan@sjtu.edu.cn

Plasseraud et al.[11] investigated tripping effects using wall-resolved large-eddy simulation (WRLES), noting that transition acceleration is effective at a 10° inclination but exhibits only localized effects at 20°. Plasseraud and Mahesh[1] subsequently expanded this scope to a wide range of Reynolds numbers and inclinations, successfully classifying wake topologies. Specialized studies by Aram et al.[12], Kumar et al.[13] further clarified the critical role of turbulent boundary layer evolution in tail flow separation, laying the groundwork for analyzing pressure fluctuations driven by boundary layer turbulence. For bluff body flow research in general, large eddy simulation has also been widely validated in canonical configurations; for example, Gao et al.[14] systematically investigated the wake characteristics of a sphere under both homogeneous and density-stratified conditions via large-eddy simulation (LES), enriching the understanding of turbulent wake evolution for bluff bodies with different geometric forms.

Despite these advancements, systematic investigations into wall pressure fluctuations within axisymmetric turbulent boundary layers remain limited, particularly regarding the interaction between convex transverse curvature and streamwise pressure gradients. Experimentally, Balantrapu et al.[15-16] measured wall pressure fluctuation spectra on a modified body of revolution. They found that as the flow decelerates near the stern, the magnitude of wall pressure fluctuations decreases concurrently with wall shear stress. Numerically, Zhou et al.[17] demonstrated that a hybrid simulation strategy, incorporating WRLES for the stern region, can achieve predictive accuracy for wall pressure fluctuations comparable to high-quality experimental measurements. Building on this, Fan et al.[18] identified robust scaling parameters via WRLES. Additionally, Chongsiripinyo et al.[19] linked wake structures to low-frequency fluctuations, while Cohen et al.[20] revealed that adverse pressure gradients enhance low-frequency components and suppress high-frequency ones. Jiang et al.[21] performed high-order large-eddy simulations on an axisymmetric underwater hull and quantitatively validated the prediction accuracy of wall pressure fluctuation spectra, confirming the reliability of LES methods in capturing turbulent pressure characteristics on revolution bodies. Wang et al.[22] investigated the separated flow around a highly inclined prolate spheroid via scale-adaptive simulation, and found that inclination-induced asymmetric boundary layer separation significantly reshapes the circumferential distribution pattern of wall pressure. Damani et al.[23] systematically characterized the sub-convective components of near-wall pressure fluctuations in turbulent boundary layers, and revealed the inherent scaling relationship between multi-scale turbulent motions and wall pressure evolution.

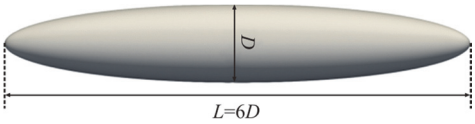


Fig. 1 Geometry of the 6:1 prolate spheroid model (L denotes the total length, D denotes the maximum cross-sectional diameter)

While existing research provides a strong foundation, three critical gaps remain. First, there is a lack of systematic comparative analysis between the 0° baseline state and moderate-to-high inclinations (such as 10° and 20°), making it difficult to quantify how continuous inclination changes affect boundary layer development and flow separation. Second, the coupling mechanism between boundary-layer transition under forced tripping and the subsequent spatiotemporal evolution of pressure fluctuations has not been thoroughly explored. Finally, a comprehensive understanding of the circumferential distribution and spectral characteristics of pressure fluctuations along the fully developed boundary layer is still missing, as most prior studies focus strictly on the wake.

To address these gaps, this study investigates a 6:1 prolate spheroid at 0°, 10°, and 20° inclinations using WRLES within the OpenFOAM platform as shown in Fig. 1. To balance computational efficiency and numerical stability, steady Reynolds-averaged Navier-Stokes simulations coupled with the k-ω shear stress transport turbulence model are initially performed on the same mesh to obtain a converged base flow field, which then initializes the unsteady WRLES. This research focuses on boundary-layer transition and development under physical tripping, systematically analyzing how inclination influences the amplitude, spatial distribution, and spectral properties of wall pressure fluctuations. Ultimately, this study aims to reveal the intrinsic coupling mechanisms linking boundary-layer transition, flow separation, and wall pressure evolution, providing high-fidelity data to support the hydrodynamic optimization and flow-induced noise control of underwater vehicles.

1. Numerical methods and validation

1.1 *Governing equations*

Given the inherent limitation of lLES in

resolving turbulent vortices across all spatial scales within the flow domain, the governing equations for LES are derived by implementing a spatial filtering operation on the incompressible Navier-Stokes equations. The filtered momentum and continuity equations are expressed as follows:

$$\frac{\partial \tilde{u}_i}{\partial t}+\frac{\partial \tilde{u}_i \tilde{u}_j}{\partial x_j}=-\frac{1}{\rho}\frac{\partial \tilde{p}}{\partial x_i}+\nu\frac{\partial^2 \tilde{u}_i}{\partial x_j \partial x_j}-\frac{\partial \tau_{ij}^{\mathrm{sgs}}}{\partial x_j} \tag{1}$$

$$\frac{\partial \tilde{u}_i}{\partial x_i}=0 \tag{2}$$

where $\tilde{u}_i$ and $\tilde{u}_{ij}$ $(i, j=1, 2, 3)$ denotes the filtered velocity component in the x_i and x_j direction, $\tilde{p}$ is the filtered pressure, ν represents the kinematic viscosity of the fluid, and τ_{ij}^{sgs} is the subgrid-scale (SGS) stress term that arises from the unresolved small-scale turbulent motions. Physically, it characterizes the momentum transport effect exerted by unresolved small-scale turbulence on the resolved large-scale flow field. The SGS stress is modelled by the eddy viscosity approach as:

$$\tau_{ij}^{\mathrm{sgs}}=2\nu_{\mathrm{sgs}}\tilde{S}_{ij}+\frac{1}{3}\tau_{kk}^{\mathrm{sgs}}\delta_{ij} \tag{3}$$

where $\tilde{S}_{ij}$ is the resolved strain rate tensor, which describes the local deformation rate of the filtered flow field, δ_{ij} is the Kronecker delta, ν_{sgs} is the SGS eddy viscosity that characterises the transport of unresolved turbulent momentum, and τ_{kk}^{sgs} is the trace of the subgrid-scale stress tensor.

In the present study, the wall-adapting local eddy viscosity (WALE) model is adopted to calculate the SGS eddy viscosity, which is particularly suitable for WRLES due to its accurate prediction of near-wall turbulent behaviours without additional wall functions[24]. The WALE model is defined as:

$$\nu_{\mathrm{sgs}}=(C_{\mathrm{w}}\Delta)^2\frac{(S_{ij}^{\mathrm{d}}S_{ij}^{\mathrm{d}})^{3/2}}{(\tilde{S}_{ij}\tilde{S}_{ij})^{5/2}+(S_{ij}^{\mathrm{d}}S_{ij}^{\mathrm{d}})^{5/4}} \tag{4}$$

where C_{w}=0.325 is the empirical WALE coefficient, Δ is the cube root of the local computational cell volume, serving as the local spatial filter width in LES, S_{ij}^{d} is the traceless symmetric part of the square of the velocity gradient tensor. As the core term of the WALE model, it integrates both shear and rotational characteristics of the local flow field. It also ensures the correct asymptotic behaviour of turbulent viscosity near the wall. This term is the key that enables the WALE model to capture near-wall vortex dynamics effectively.

1.2 *Computational domain and mesh*

The physical system considered is sketched schematically in Fig. 2.

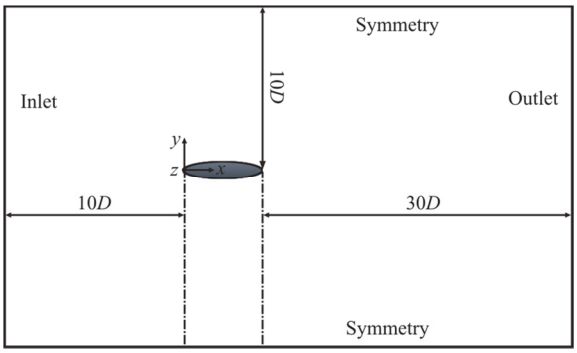


Fig. 2 Computational domain

The total number of cells is 1.40×10^8. Details of the mesh are depicted in Fig. 3. To satisfy WRLES requirements, the wall-normal height of the first cell is set at $y^+=0.8$ (y^+ is the dimensionless wall-normal distance), with 50 layers distributed within the boundary layer. Streamwise and spanwise resolutions are maintained at $\Delta x^+=80$ and $\Delta z^+=80$, respectively. This configuration ensures sufficient fidelity to capture both near-wall turbulent structures and wall pressure fluctuations.

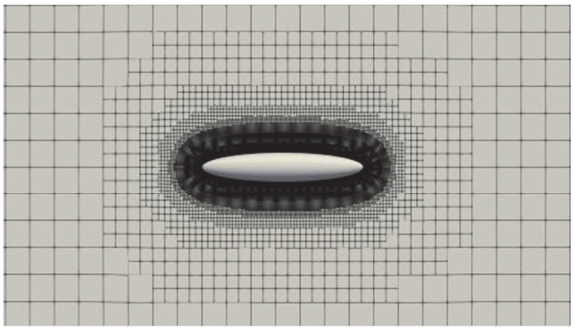
In this work, a physical trip wire is installed at the streamwise location $x/L=0.2$ (x is the streamwise distance from the nose) on the forebody of the prolate spheroid to trigger boundary layer transition to turbulence. The trip wire is configured as a ring normal to the wall, with a streamwise width of 1 mm and a height of 2 mm (corresponding to dimensionless values $w/D\approx0.004\,4$ and $h/D\approx0.008\,7$, where w is the streamwise width of the trip wire and h is its height, normalized by the maximum diameter D of the prolate spheroid). An identical computational grid for the prolate spheroid is adopted for all cases with different AOAs, and the detailed configuration of the physical trip wire is illustrated in Fig. 4.

1.3 *Solvers and computational matrix*

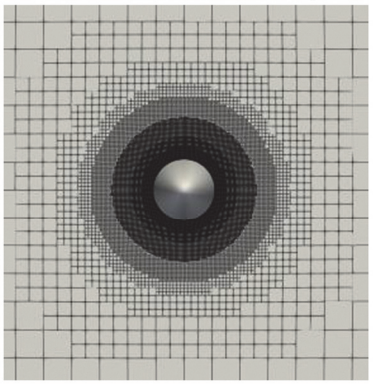
All numerical simulations in this work are performed using the open-source CFD platform OpenFOAM, which is widely adopted in academic research for its flexible framework in turbulent flow computations. The governing equations are discretized with the cell-centred finite volume method, and the incompressible continuity and momentum equations are solved in the present study.

The full computational matrix for the simulations is listed in Table 1. Three groups of simulations are conducted in this study, corresponding to AOAs of

0°, 10°, and 20°. The Reynolds number (Re) for all simulations is fixed at 4.2×10^6.



(a) Mesh distribution on the z=0 plane



(b) Mesh distribution on the x=0.5L plane

Fig. 3 Details of the mesh

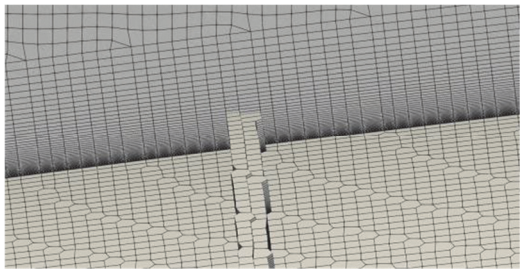


Fig. 4 Form of the physical trip wire

Table 1 Computational matrix

Re	α
4.2×10^6	0°
4.2×10^6	10°
4.210^6	20°

1.4 *Grid independence verification*

For the global computational grid of the prolate spheroid, a geometric progression meshing strategy is adopted for fine refinement. This ensures that the near-wall grid accurately resolves the flow characteristics within the boundary layer. In the numerical simulation of flow around the prolate spheroid, accurate capture of boundary layer development and effective extraction of wall fluctuating pressure are highly sensitive to the grid resolution in the streamwise (x- direction) and spanwise (z- direction). Therefore, grid accuracy in both x- and z- directions must be given priority in the grid convergence verification of this section. The systematicness and rigor of the grid convergence verification must be guaranteed. For this purpose, the dimensionless grid resolutions (Δx^+, Δz^+) in the two directions are increased at the same proportional rate, and the refinement ratio is set to $\sqrt[3]{2}$. Based on this strategy, three systematic grid systems are established, namely the coarse grid (89×10^6 cells), the medium grid (1.4×10^8 cells), and the fine grid (1.8×10^8 cells).

As shown in Fig. 5, good grid convergence of hydrodynamic characteristics is achieved for the numerical simulation of flow around the prolate spheroid. Comparative analysis of three grid resolutions (coarse, medium, and fine) reveals that after the flow field is fully developed, the streamwise distribution of the wall pressure coefficient C_p follows a consistent overall trend, with very low sensitivity to grid refinement. Upstream of the trip wire, the C_p curves for all three grids are nearly identical. However, at the trip wire and in its downstream region, clear differences are observed between the coarse grid results and those of the medium and Fine grids. Specifically, the coarse grid significantly underestimates the wall pressure at the trip wire. In the downstream region after boundary layer transition, the coarse grid also produces a spurious pressure peak and slightly underestimates the wall pressure. The C_p curves from the Medium and Fine grids are nearly identical, and both sets of results are in good agreement with experimental measurements. In summary, grid independence verification confirms that the medium grid (1.4×10^8 cells) is the optimal choice for the numerical simulation. It balances computational efficiency while ensuring accurate calculation of hydrodynamic characteristics.

$$C_p = \frac{p - p_\infty}{0.5\rho U_\infty^2} \tag{5}$$

where p is the local static pressure on the body surface, p_∞ denotes the freestream static pressure, ρ represents the fluid density, and U_∞ is the freestream velocity magnitude.

1.5 *Validation of present WRLES*

To validate the accuracy of the present numerical method, Fig. 6 shows the normal force and pitch moment coefficients on a prolate spheroid for various AOAs, which are defined as:

$$C_Z = \frac{N}{qS}, C_M = \frac{M}{qSL_r} \tag{6}$$

where N is the normal force perpendicular to the free-stream velocity, M is the pitching moment about the geometric center of the prolate spheroid, q is the free-stream dynamic pressure, S is the frontal area of the model, namely the maximum cross-sectional area perpendicular to the major axis of the prolate spheroid, and L_r is the reference length of the prolate spheroid.

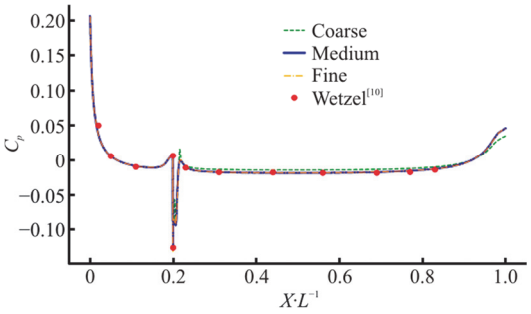


Fig. 5 Surface pressure coefficient (C_p) distributions for three grid sets

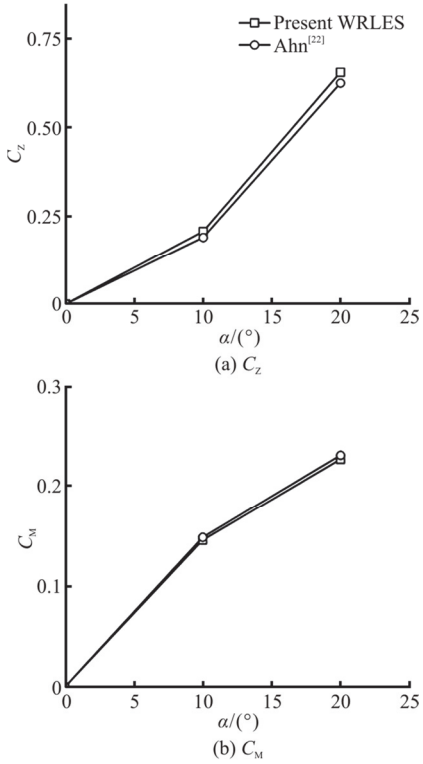


Fig. 6 Normal force and pitch moment on prolate spheroid for various AOAs

As shown in Fig. 6, the C_Z and C_M of the prolate spheroid obtained by the WRLES agree well with the experimental data of Ahn[25]. Both coefficients increase approximately linearly with the AOA over the range of $0°$ to $20°$. At low AOA, the flow is dominated by attached flow, so the force and moment vary gently. As the AOA rises, flow separation and vortex development on the leeward side speed up the growth of loads, and the overall trend is highly consistent with the experiment. Combined with the good agreement of the surface pressure coefficient C_p with experimental data in the previous grid independence verification, these results prove that the numerical method in this paper can accurately capture the flow field and load characteristics at different AOAs, thus verifying its reliability.

2. Results and discussion

2.1 *Overview of the flow fields*

Figure 7 presents the instantaneous three-dimensional vortex structures near the wall of the prolate spheroid at three AOAs, extracted using the Liutex vortex identification method[26]. As the core metric of the Liutex method, the dimensionless vortex strength parameter Ω_R is defined based on the pure rigid-body rotational component of the local velocity gradient tensor, which quantitatively characterizes the rotational intensity of the local flow field. The iso-surfaces are extracted at a threshold of $\Omega_R = 10$ to retain dominant turbulent vortex structures with significant rotational properties, and are colored by streamwise velocity (U_{mean}).

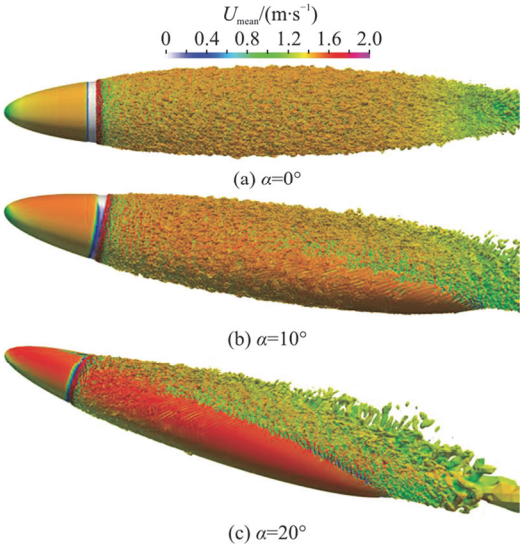


Fig. 7 Instantaneous near-wall vortical structures at three AOAs $(\Omega_R = 10)$

The vortex structures show that the physical tripping wire initiates a rapid transition from laminar to turbulent flow, and the near-wall turbulence also exhibits multi-scale characteristics. Along the streamwise direction, the turbulent boundary layer develops continuously, the vortex structures attached to the prolate spheroid grow rapidly, and this drives a notable increase in the boundary layer thickness. In

the trailing region of the prolate spheroid, the adverse pressure gradient triggers flow separation, forming a wake region with a dense distribution of vortical structures. It is also observed that an increase in the AOA (α) significantly suppresses the transition-promoting effect of the physical tripping wire. As α increases from 0° to 20°, the boundary layer transition effect downstream of the tripping wire on the windward side deteriorates progressively, and the non-transitional region is concentrated on the windward side of the aft half of the prolate spheroid. Within the α range of 0° to 20°, the area of the non-transitional region increases monotonically with rising AOA, and this finding is consistent with the conclusions reported by Plasseraud et al.[11].

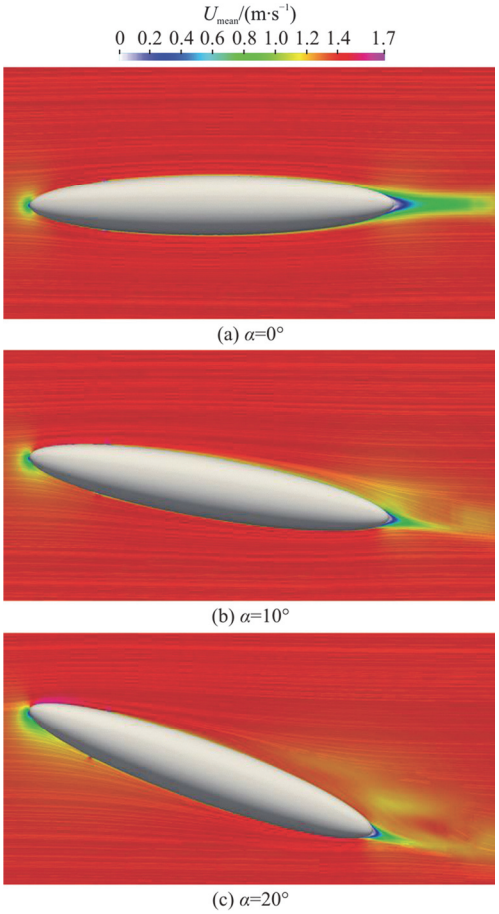


Fig. 8 Time-averaged flow field of U_{mean} with streamlines at three AOAs

Figures 8, 9 present the time-averaged streamwise velocity field (superimposed with streamlines) and instantaneous wall pressure field around the prolate spheroid under a range of AOA. For the baseline 0° AOA case, the flow maintains perfect axisymmetry, with streamlines adhering smoothly to the entire body surface and a narrow symmetric wake formed downstream, in the corresponding pressure field, the stagnation point at the nose corresponds to a high-pressure region, an adverse pressure gradient (APG) develops along the streamwise direction of the nose section, the mid-body exhibits an approximately zero pressure gradient (ZPG), and pressure recovers smoothly toward the trailing edge. With increasing AOA, this axisymmetric flow structure is completely broken: In the velocity field, a steeper velocity gradient forms on the windward side with streamlines remaining fully attached, while in contrast, flow velocity decreases sharply on the leeward side accompanied by clear flow separation and streamline detachment; correspondingly, the pressure field undergoes asymmetric reconstruction, with the high-pressure region originally at the nose stagnation point shifting toward the windward side, a distinct favorable pressure gradient (FPG) forming in the upstream segment of the windward side and transitioning to an APG in the downstream segment, while the pressure gradient distribution on the leeward side follows the opposite trend.

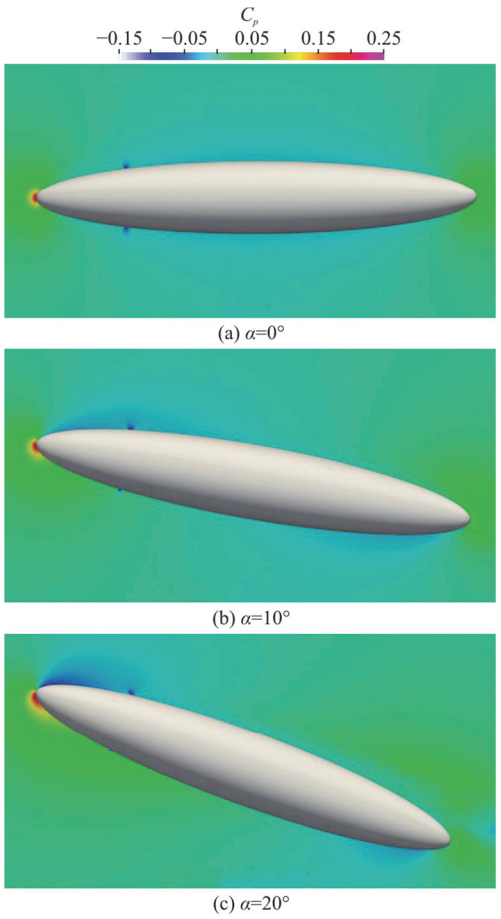


Fig. 9 Instantaneous flow field of pressure at three AOAs

Meanwhile, the evolution of pressure fluctuations also shows a clear asymmetric pattern with increasing AOA: Fluctuation intensity is greatly weakened on the

windward side and enhanced on the leeward side. Notably, the spatial distribution range of pressure fluctuations is significantly narrower than that in the 0° AOA case, and contracts progressively toward the trip wire as AOA increases. This flow field evolution is primarily driven by the asymmetric circumferential pressure gradient distribution induced by AOA, and the differentiated pressure gradients on the windward and leeward sides directly regulate boundary layer stability and turbulent fluctuation characteristics.

Figure 10 presents the boundary layer thickness distributions along the major axis on the lateral, windward, and leeward sides of the prolate spheroid at three AOAs. All observed differences across AOA are fundamentally driven by redistributed streamwise and circumferential surface pressure gradients induced by flow incidence changes, which govern boundary layer development, fluid transport, and separation.

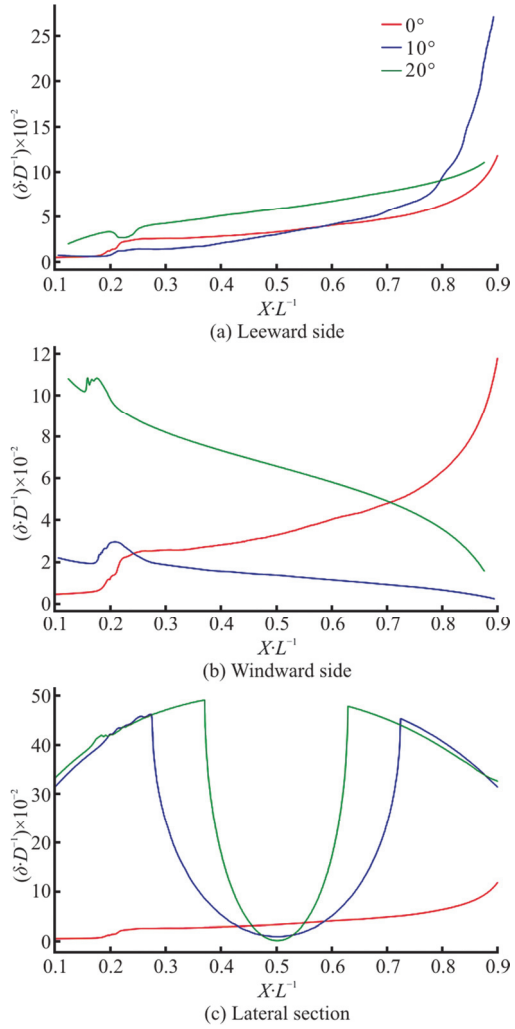


Fig. 10 Boundary layer thickness distribution along the major axis of the prolate spheroid at different AOAs

For the lateral section, the flow is axisymmetric with uniform circumferential pressure at 0° AOA. An abrupt thickness increase at $x/L=0.2$ is solely due to the trip wire-induced transition. At 10° and 20° AOA, asymmetric incidence creates strong circumferential and modified streamwise pressure gradients on the lateral side, producing a U-shaped thickness distribution: Initial thickening under mild adverse pressure gradient, sharp drop to a minimum near $x/L\approx 0.5$ (primary separation line), then re-thickening. Increasing AOA shifts the pressure gradient distribution downstream, moving the separation line aft and narrowing the minimum thickness interval.

On the windward side, the trip wire causes abrupt thickening at $x/L=0.2$ for all AOAs. AOA generates a strong, favorable streamwise pressure gradient that accelerates the boundary layer and suppresses thickening, plus a circumferential pressure gradient driving cross-flow that transports low-momentum fluid to the leeward side. Their combined effect results in a continuous streamwise thinning, with the rate increasing with AOA as both gradients intensify.

On the leeward side, trip wire-induced thickening occurs at $x/L=0.2$ at 0° and 10° AOAs. At 20° AOA, severe asymmetric pressure shifts the stagnation point windward, displacing the leeward trip wire downstream and creating a thinner laminar region upstream. Non-zero AOA produces a dominant adverse streamwise pressure gradient, which, together with accumulated low-momentum fluid from cross-flow, causes dramatic thickening. Explosive thickening occurs at $x/L>0.7$ at 10° AOA (tail separation), while earlier separation at 20° AOA leads to gradual thickening without a distinct peak.

2.2 *Analysis of wall pressure fluctuations*

In this section, the spectral characteristics and spatial evolution of wall pressure fluctuations over a tripped prolate spheroid at various AOAs are investigated. The one-sided power spectral density (PSD) of the wall pressure fluctuations at each monitoring point was computed by applying a discrete Fourier transform to the single-point fluctuating pressure time-history data. To effectively mitigate spectral leakage during signal processing, the time series was divided into segments with a 50% overlap, and a Hanning window was applied for smoothing.

To accurately capture the axial evolution characteristics of the flow field, a series of monitoring points was positioned on the surface of the spheroid, as illustrated in Fig. 11. The total length of the prolate spheroid model is 54 inches ($L=1.3716$ m). The measurement points were distributed axially, both

upstream and downstream of the trip wire. Detailed axial positions and corresponding dimensionless coordinates x/L of all monitoring points are summarized in Table 2.

Table 2 Axial coordinates of monitoring points

Monitoring point	x/L
M1	0.148
M2	0.185
M3	0.222
M4	0.370
M5	0.500
M6	0.593
M7	0.741
M8	0.963

All PSD spectra presented in this section were derived from the data collected at these specific locations. Furthermore, under all evaluated angle-of-attack conditions, the identical set of monitoring points was symmetrically deployed along both the windward and leeward axial lines of the spheroid to comprehensively monitor and compare variations in wall pressure fluctuations across different flow-separation regimes.



Fig. 11 Arrangement of measurement locations (M1-M8)

As shown in Fig. 12, the PSD of wall pressure fluctuations on the windward side exhibits clear axial non-uniformity under different AOAs, which is directly modulated by the streamwise evolution of the windward pressure gradient and its interaction with the trip wire.

In the upstream region before the trip wire (M1-M2), PSD remains low and smooth at 0° and 10° AOA, indicating a low-disturbance boundary layer. At 20° AOA, however, PSD at M2 increases significantly, with energy levels approaching post-transition states in some frequency bands. This is because the windward FPG extends upstream with increasing AOA, promoting disturbance amplification ahead of the trip wire. Consequently, the transition influence extends toward the nose, and the effective trip wire region shifts upstream.

Downstream of the trip wire (M3), all cases show a sharp PSD increase, confirming the trip wire's triggering effect. However, transition behavior differs with AOA due to varying pressure gradient strengths. At 0° AOA (near ZPG), the PSD rise from M2 to M3 is most pronounced, indicating abrupt transition. At 20° AOA, the strong FPG enhances boundary layer stability, weakening the trip wire's role as a localized forcing source. Combined with elevated upstream disturbances, this reduces the PSD difference between M2 and M3, making the transition process more gradual and spatially broadened.

This trend becomes more evident in the mid-downstream region (M4-M7), where PSD generally follows $0° > 10° > 20°$, especially at low frequencies. The difference between 0° and 10° is small, while that between 10° and 20° is much larger, indicating a nonlinear pressure gradient effect on flow stability. The persistent FPG on the windward side suppresses turbulent kinetic energy generation and development, leading to insufficient turbulence downstream and reduced wall pressure fluctuations at higher AOA. This reflects a shift from localized forced transition (0° AOA) to a more distributed, gradual transition process (20° AOA) modulated by the FPG.

At the rear location (M8), the trend reverses: PSD at 20° AOA is significantly higher than at 0° and 10°. Although mid-downstream transition is suppressed by the FPG, boundary layer instabilities accumulate along the streamwise direction and are abruptly released by the strong APG near the stern. This generates large-scale vortical structures and intense unsteady motion, enhancing the low-frequency energy of wall pressure fluctuations. In contrast, earlier transition at lower AOA results in more uniform rear flow and weaker unsteadiness.

Overall, the windward pressure gradient exerts a dual control on trip-wire-induced transition and pressure fluctuations: The upstream FPG promotes disturbance growth and shifts transition forward, while suppressing the trip wire's localized forcing effect and mid-downstream turbulence; the downstream APG triggers the release of accumulated instabilities, enhancing rear low-frequency fluctuations. This results in the characteristic PSD pattern of "upstream shift, mid-region attenuation, and rear enhancement".

As shown in Fig. 13, the leeward wall pressure fluctuation PSD exhibits distinct axial evolution patterns compared to the windward side, driven by the opposite pressure gradient sequence on the leeward surface.

In the upstream region (M1-M2), the trend shows stronger AOA dependence than the windward side. At M1, PSD at 20° AOA is already significantly higher than at 0° and 10°, because the leeward APG propagates upstream more effectively than the windward FPG, enhancing boundary layer disturbances closer to the nose. Consequently, the trip wire's influence region extends further upstream on the leeward side than on the windward side. At M3, PSD at 0° and

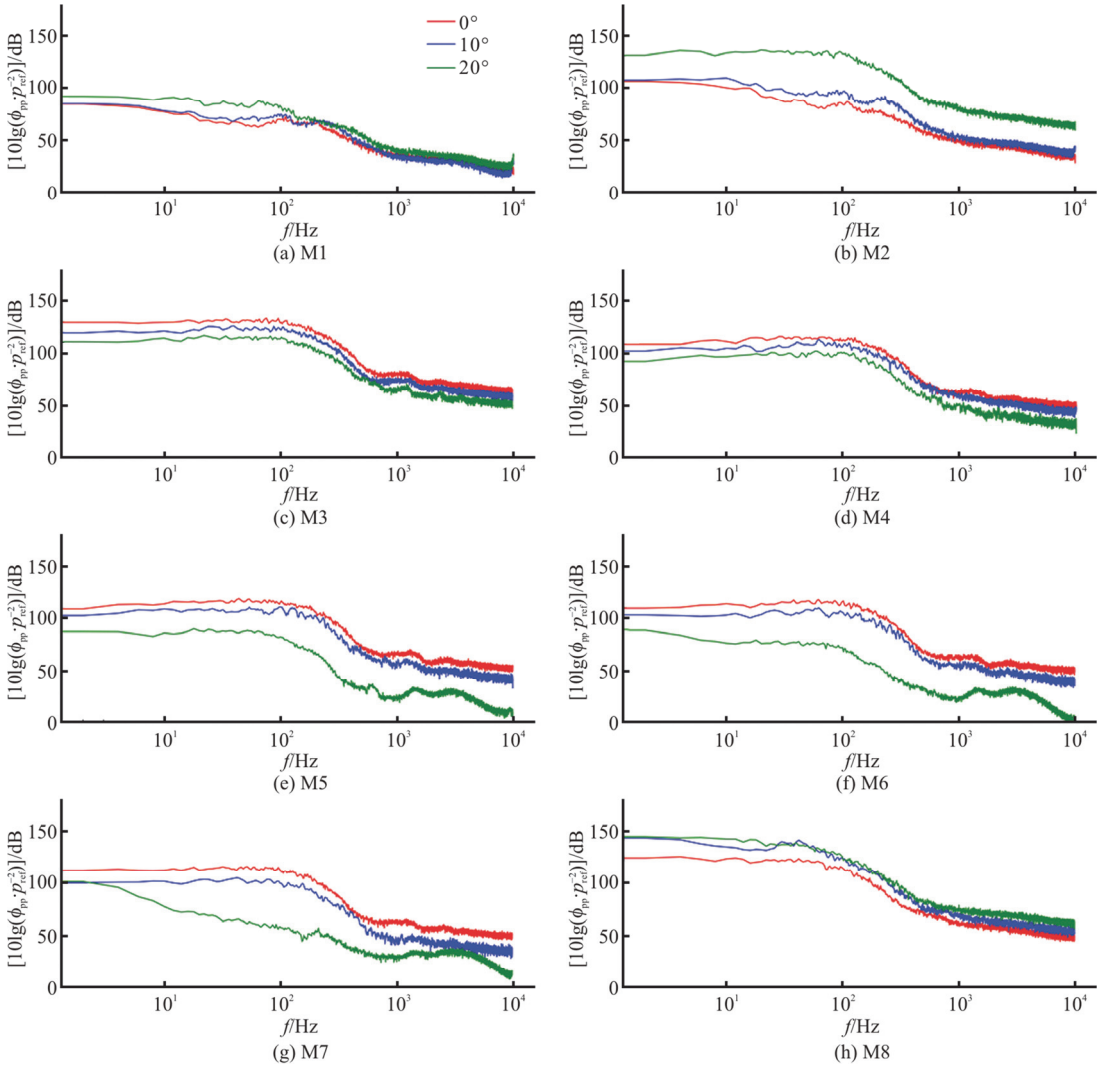


Fig. 12 Evolution of wall pressure fluctuation frequency spectra: effects of different AOAs and monitoring points (M1-M8) on the windward side (f is the frequency, ϕ_{pp} is the power spectral density of wall pressure fluctuations, and p_{ref} is the reference pressure)

10° AOA exceed that at 20° , indicating that although upstream disturbances are enhanced by the APG, the trip wire's transition-triggering effect is still suppressed at high AOA. This behavior is consistent with the windward side, suggesting that increasing AOA weakens the trip wire's role as a localized strong disturbance source and promotes a shift from abrupt to gradual transition. However, unlike the windward side, this suppression effect is limited to the near-field immediately downstream of the trip wire.

Further downstream (M4-M7), PSD curves at different AOAs rapidly converge, and AOA influence becomes negligible. In this region, the strong leeward APG induces flow separation, and the flow quickly transitions from transition-dominated to separated shear layer-dominated. The unsteady characteristics are now controlled by shear layer instabilities, which exhibit self-similar behavior independent of upstream transition intensity or AOA. Although AOA modifies upstream disturbances and near-trip transition, these effects are rapidly dissipated and reorganized by the nonlinear evolution of the shear layer, leading to nearly identical statistical behavior across all cases.

At the rear location (M8), only minor differences between AOA cases are observed with no clear trend. This confirms that the leeward flow reaches a statistically stable state dominated by the separated shear layer before entering the wake, and the influence of AOA on wall pressure fluctuations is fully diminished.

Overall, leeward PSD evolution exhibits a clear three-stage behavior modulated by the APG: upstream enhancement (APG amplifies pre-trip disturbances and shifts trip influence forward), local suppression (APG weakens near-trip transition triggering), and downstream attenuation (separated shear layer dominates

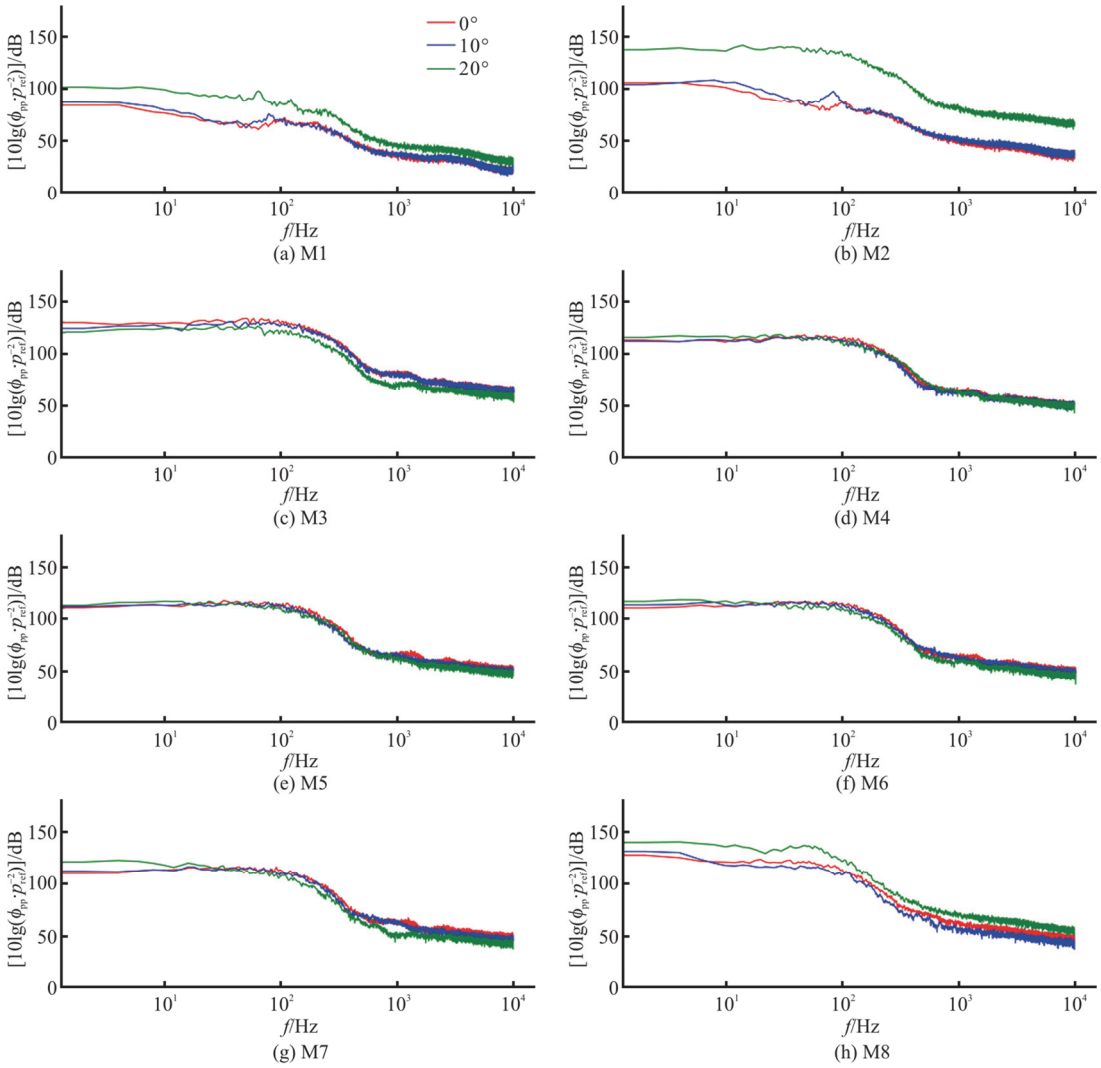


Fig. 13 Evolution of wall pressure fluctuation frequency spectra: Effects of different AOAs and monitoring points (M1-M8) on the leeward side

and dissipates AOA effects). This "upstream enhancement-local suppression-downstream attenuation" pattern is the key distinguishing feature between leeward and windward pressure fluctuations.

A combined analysis of Figs. 12, 13 reveals that the fundamental difference in wall pressure fluctuation responses between windward and leeward sides originates from their opposite pressure gradient distributions:

On the windward side, the dominant FPG maintains boundary layer attachment, making the flow transition-controlled. At low AOA (near ZPG), the trip wire effectively triggers abrupt transition. As AOA increases, the strengthening FPG extends upstream, enhancing pre-trip disturbances while weakening the trip wire's localized triggering strength. This results in a more gradual transition process and the characteristic $0° > 10° > 20°$ PSD magnitude pattern in the mid-downstream region. On the leeward side, the dominant APG rapidly induces flow separation, making the flow separation-dominated. Although the APG also enhances upstream disturbances and suppresses near-trip transition, its primary effect is to trigger the formation of a separated shear layer. The nonlinear evolution of shear layer instabilities quickly dissipates any upstream AOA effects, leading to converged PSD distributions and overall weak sensitivity to AOA in the mid and downstream regions.

Therefore, the windward side exhibits a "transition-controlled" response modulated by FPG, while the leeward side exhibits a "separation-dominated" response modulated by APG. This pressure gradient-driven mechanism difference determines the spatial distribution of wall pressure fluctuations under varying AOA conditions.

3. Conclusions

In this study, WRLES are performed to investigate the flow characteristics and wall pressure fluctuations over a 6:1 prolate spheroid with a physical trip wire, at $Re = 4.2 \times 10^6$. The key findings are summarized as follows:

(1) Flow field and boundary layer development

Increasing AOA induces circumferentially asymmetric pressure gradients, which destroy the mean flow axisymmetry and drive strong cross-flow motions. On the windward side, the FPG enhances boundary layer stability, weakening the trip wire's localized forced transition effect and leading to a more gradual transition process; combined with cross-flow transport of low-momentum fluid toward the leeward side, this results in continuous windward boundary layer thinning. On the leeward side, the APG destabilizes the boundary layer, and cross-flow accumulation of low-momentum fluid leads to pronounced boundary layer thickening and earlier flow separation.

(2) Windward wall pressure fluctuations

The windward FPG modulates trip wire-induced transition and pressure fluctuation evolution: It weakens the trip wire's localized forcing effect and suppresses mid-body turbulent development, directly reducing pressure fluctuation intensity in the mid-body region. Conversely, the strong adverse pressure gradient near the stern triggers the abrupt release of streamwise-accumulated boundary layer instabilities, significantly amplifying low-frequency unsteadiness in the near-stern region.

(3) Leeward wall pressure fluctuations

The leeward APG dominates the flow evolution: Although it enhances initial disturbance amplitudes in the upstream leeward region, it rapidly induces flow separation and the formation of a self-similar separated shear layer. The nonlinear evolution of shear layer instabilities dissipates all upstream AOA effects, leading to rapid convergence of mid-to-downstream pressure fluctuation spectra and rendering leeward wall pressure fluctuations largely insensitive to AOA variations.

Conflict of interest

All authors declare that there are no other competing interests.

References

[1] Plasseraud M, Mahesh K. Vortex topology in the lee of a 6:1 prolate spheroid [J]. *Journal of Fluid Mechanics*, 2025, 1024: A22.

[2] Chesnakas C J, Simpson R L. Full three-dimensional measurements of the cross-flow separation region of a 6:1 prolate spheroid [J]. *Experiments in Fluids*, 1994, 17(1): 68-74.

[3] Xiao Z, Zhang Y, Huang J, et al. Prediction of separation flows around a 6:1 prolate spheroid using RANS/LES hybrid approaches [J]. *Acta Mechanica Sinica*, 2007, 23(4): 369-382.

[4] Wikström N, Svennberg U, Alin N, et al. Large eddy simulation of the flow around an inclined prolate spheroid [J]. *Journal of Turbulence*, 2004, 5(1): 029.

[5] Meier H U, Kreplin H P, Vollmers H. Development of boundary layers and separation patterns on a body of revolution at incidence [C]//*Proceedings of the 2nd Symposium on Numerical and Physical Aspects of Aerodynamic Flows*, Long Beach, USA, 1983.

[6] Liu J, An D, Zhu J, et al. Vortex dynamics mechanism of the staggered impeller suppressing pressure fluctuations in a double-suction centrifugal pump [J]. *Journal of Hydrodynamics*, 2025, 37(2): 209-229.

[7] Ohh C Y, Spedding G R. The effects of stratification on the near wake of 6:1 prolate spheroid [J]. *Journal of Fluid Mechanics*, 2024, 997: A43.

[8] Fu T C, Shekarriz A, Katz J, et al. The flow structure in the lee of an inclined 6:1 prolate spheroid [J]. *Journal of Fluid Mechanics*, 1994, 269: 79-106.

[9] Meier H U, Kreplin H P. Experimental investigation of the boundary layer transition and separation on a body of revolution [J]. *Zeitschrift fur Flugwissenschaften und Weltraumforschung*, 1980, 4: 65-71.

[10] Wetzel T G. Unsteady flow over a 6:1 prolate spheroid [D]. Doctoral Thesis, Blacksburg, USA: Virginia Polytechnic Institute and State University, 1996.

[11] Plasseraud M, Kumar P, Mahesh K. Large-eddy simulation of tripping effects on the flow over a 6:1 prolate spheroid at angle of attack [J]. *Journal of Fluid Mechanics*, 2023, 960: A3.

[12] Aram S, Shan H, Jiang L, et al. Numerical analysis of natural boundary layer transition and trip effect on inclined spheroid [C]//*AIAA Scitech 2022 Forum*, San Diego, USA, 2022.

[13] Kumar P, Mahesh K. Large-eddy simulation of flow over an axisymmetric body of revolution [J]. *Journal of Fluid Mechanics*, 2018, 853: 537-563.

[14] Gao G, Wang Y, Cao L, et al. Large eddy simulation of the wake behind a sphere with and without density stratification at *Re* = 3 700 [J]. *Journal of Hydrodynamics*, 2024, 36(6): 1009-1020.

[15] Balantrapu N A, Fritsch D J, Millican A J, et al. Wall pressure fluctuations in an axisymmetric turbulent boundary layer under strong adverse pressure gradient [C]//*AIAA Scitech 2020 Forum*, Orlando, USA, 2020.

[16] Balantrapu N A, Alexander W N, Devenport W. Wall-pressure fluctuations in an axisymmetric boundary layer under strong adverse pressure gradient [J]. *Journal of Fluid Mechanics*, 2023, 960: A28.

[17] Zhou D, Wang K, Wang M. Large-eddy simulation of an axisymmetric boundary layer on a body of revolution [C]//*AIAA Aviation 2020 Forum*, Orlando, USA, 2020.

[18] Fan G, Chen H, Zhao W, et al. Scaling laws and space-time characteristics of wall pressure fluctuations in an axisymmetric boundary layer with varying pressure gradient [J]. *Journal of Fluid Mechanics*, 2025, 1016: A28.

[19] Chongsiripinyo K, Sarkar S. Decay of turbulent wakes behind a disk in homogeneous and stratified fluids [J]. *Journal of Fluid Mechanics*, 2020, 885: A31.

[20] Cohen E, Gloerfelt X. Influence of pressure gradients on

wall pressure beneath a turbulent boundary layer [J]. *Journal of Fluid Mechanics*, 2018, 838: 715-758.
[21] Jiang P, Liao S, Xie B. Large-eddy simulation of flow noise from turbulent flows past an axisymmetric hull using high-order schemes [J]. *Ocean Engineering*, 2024, 312: 119150.
[22] Wang B, Lin X, Liu H, et al. Scale-adaptive simulation of the separated flow past a 90°-inclined prolate spheroid [J]. *Physics of Fluids*, 2024, 36(4): 045101.
[23] Damani S, Butt H, Totten E, et al. Measurement and analysis of sub-convective wall pressure fluctuations in turbulent boundary layer flows [J]. *Journal of Fluid Mechanics*, 2025, 1014: A26.
[24] Nicoud F, Ducros F. Subgrid-scale stress modelling based on the square of the velocity gradient tensor [J]. *Flow, Turbulence and Combustion*, 1999, 62(3): 183-200.
[25] Ahn S. An experimental study of flow over a 6 to 1 prolate spheroid at incidence [D]. Doctoral Thesis, Blacksburg, USA: Virginia Polytechnic Institute and State University, 1992.
[26] Liu C, Gao Y, Dong X, et al. Third generation of vortex identification methods: Omega and Liutex/Rortex based systems [J]. *Journal of Hydrodynamics*, 2019, 31(2): 205-223.